(Received 14 January 2026, Accepted 12 February 2026, Scheduled 2 March 2026)

A Wideband Dual-CP Antenna with Low-Profile Based on Distributed Coupling for Coal Mine Communication

Lei Li[1,2,*], Xiaomeng Wang[1,2], Yuting Jia[1,2], Yanting Wang[1,2], Hongyu Zhang[1,2], and Jingchang Nan[1,2]

[1]*School of Electronics and Information Engineering, Liaoning Technical University, Huludao 125105, China*
[2]*Liaoning Key Laboratory of Radio Frequency and Big Data for Intelligent Applications, Huludao 125105, China*

ABSTRACT: This study presents a wideband dual-circularly polarized (dual-CP) antenna based on a distributed electromagnetic coupling mechanism. The antenna employed a circular slot structure fed by dual L-shaped microstrip lines. By introducing a rectangular protrusion on the ground plane and splitting it with a narrow slit, multiple parallel radiating paths were formed, establishing a distributed coupling mechanism. This mechanism introduces multiple resonant points to extend the impedance bandwidth (IBW) and generates multiple orthogonal components to enhance the axial ratio bandwidth (ARBW). The dual-port, left-right symmetric configuration enables dual-CP operation. The narrow slit decouples the shared current paths between the feeding structures, further enhancing the port isolation. Owing to its single-layer structure, the fabricated antenna achieves a low profile of only $0.011\lambda_0$. Measured results show an IBW of 87.8% (2.98–7.65 GHz) and an ARBW of 66.9% (2.72–5.47 GHz). The proposed antenna achieves a wide bandwidth and low profile simultaneously, featuring a simple and easy-to-manufacture structure. Its operating band meets the requirements for coal mine communication systems.

1. INTRODUCTION

Underground mine tunnels represent confined, heterogeneous, nonuniform, and time-varying communication spaces. During propagation within a mine, electromagnetic waves undergo reflection, scattering, and diffraction, leading to multipath effects and consequent signal fading. Moreover, the irregular presence of coal seam water mist significantly increases signal multipath reflection and attenuation, severely degrading the communication quality [1–3]. In contrast, circularly polarized (CP) antennas effectively mitigate multipath interference owing to their inherent polarization rotational characteristics, thus improving communication reliability and stability underground [4–6]. In addition, as smart coal mine construction advances, the growing number of underground devices has intensified the need for multi-band wireless communication. Intelligent development has driven the widespread adoption of portable mining equipment. Consequently, CP wideband antennas with low profile are suitable for portable communications.

Common designs for wideband CP antennas include microstrip patch antennas [7–9], slot antennas [10–12], metasurface (MS) antennas [13–15], and cross-dipole antennas [16–18]. All of them can demonstrate favorable CP performance. However, they only achieved a single CP. During underground propagation, signals are easily reflected by obstacles. In comparison, dual-circularly polarized (dual-CP) antennas support both left-hand circular polarization (LHCP) and right-hand circular polarization (RHCP), effectively mitigating the polarization reversal induced by multipath reflection, thus enhancing communication reliability. Dual-CP antennas can be categorized into two types according to the feeding port: single-port [19–22] and dual-port [23–30]. To achieve dual-CP within the same frequency band, single-port antennas typically require switching components, such as PIN diodes, to control the polarization, whereas dual-port antennas depend on different excitations. Ref. [23] used two pairs of differential ports fed through 90° hybrid couplers. Exciting the first or second pair established a phase sequence of (0°, 270°, 180°, 90°) or (0°, 90°, 180°, 270°) on the L-shaped probes, respectively. This excited two degenerate cavity modes with equal amplitude and a ±90° phase shift, yielding LHCP or RHCP radiation. Ref. [24] proposed a dual-CP antenna fed by a single-section hybrid coupler. The coupler excites two orthogonal modes in a stacked patch through aperture coupling. It provides an equal amplitude and a 90° phase difference between them. Switching the excitation port reversed this phase difference, which enabled the generation of dual-CP waves. In [26], a crossed-dipole antenna was excited by a sophisticated feeding network that integrated an orthogonal wideband coupler with parallel transmission lines. This network equally divides the input signal and applies phase shifts, thereby creating a rotating current sequence with successive 90° phase differences across the four dipole arms to radiate CP radiation. Reversing the excitation port flips the phase sequence, which generates either the LHCP or RHCP. Ref. [27] proposed a transmissive array element based on magnetoelectric dipoles, which achieves dual-CP and independent beam control within the same frequency band. The element adopts a back-to-back dual-polarized magnetoelectric dipole design connected via equal-length transmission lines, resulting in a handedness inversion of the transmitted CP wave

* Corresponding author: Lei Li (lntuicgroup@163.com).

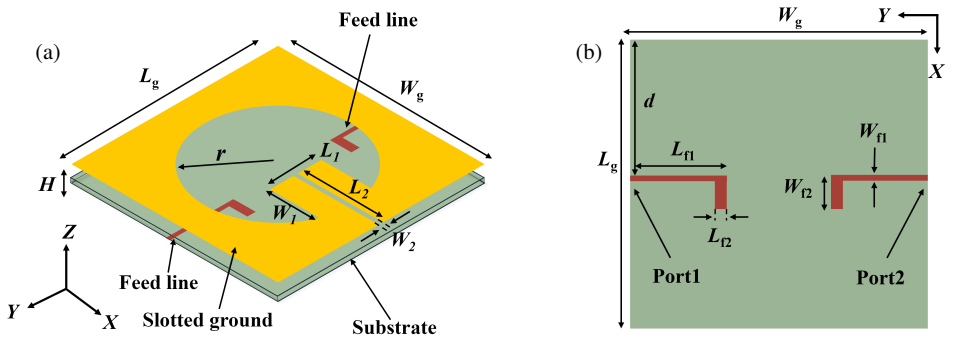

FIGURE 1. Configuration of the proposed antenna. (a) 3D view. (b) Feed-network ($L_g = W_g = 40\,\text{mm}$, $r = 14\,\text{mm}$, $L_1 = 10\,\text{mm}$, $W_1 = 12\,\text{mm}$, $W_2 = 2\,\text{mm}$, $L_2 = 18\,\text{mm}$, $L_{f1} = 13\,\text{mm}$, $W_{f1} = 0.8\,\text{mm}$, $L_{f2} = 2\,\text{mm}$, $W_{f2} = 4\,\text{mm}$, $H = 0.8\,\text{mm}$, $d = 19, 6\,\text{mm}$).

(e.g., LHCP converted to RHCP). Ref. [28] proposes an MS antenna consisting of a cross-slot coupled structure and a 4×4 square metal patch. Through characteristic mode analysis, two degenerate modes were selected and excited, generating the CP. Two orthogonally placed microstrip lines enable excitation of the LHCP and RHCP.

To achieve a wide bandwidth, existing approaches often introduce additional resonances or wideband feeding networks. For instance, using a differential feeding network with wideband 90° hybrid couplers, Ref. [23] simultaneously excited two degenerate modes via L-shaped probes. This provided stable quadrature excitation across a wide band, yielding a 28.6% axial ratio bandwidth (ARBW); optimizing the probe-cavity coupling further achieved a 29% impedance bandwidth (IBW). Ref. [24] combined multiple resonances using stacked patches and aperture coupling, achieving a 30.9% IBW and 29.1% ARBW. In [26], a design employing two pairs of vertical parallel transmission lines and an air layer achieved a 104% IBW, while an integrated orthogonal wideband coupler extended the ARBW to 100%. However, these structures generally exhibit high profiles, potentially limiting their application in spatially constrained environments. To address this limitation, researchers have designed wideband dual-CP antennas using an MS, which offers inherent wideband properties and low-profile. In [28], a modified slot structure was used to introduce an additional resonant point, combined with the intrinsic resonance of the MS. This approach expanded the IBW to 52.5% and achieved an ARBW of 31.3%, while maintaining a low profile of $0.04\lambda_0$. Additionally, slot antennas are also commonly employed in wideband dual-CP designs, as they predominantly feature single-layer, low-profile structures [29, 30]. Both designs employ a coplanar waveguide (CPW) feed to maintain the low-profile configuration. The design in [29] utilizes an asymmetric T-shaped feed and a composite grounding strip to excite multi-path resonances, yielding multiple resonant frequencies and minimum axial ratio (AR) points. With a profile of $0.016\lambda_0$, it achieves an 81.7% IBW and a 59.65% ARBW. Similarly, Ref. [30] employs an L-shaped ground plane and arrow-shaped strips to generate CP radiation and bandwidth enhancement, achieving a 108.9% IBW and a 92.6% ARBW at a profile of only $0.006\lambda_0$.

To meet the requirements for portable coal mine communication devices, this study proposes a wideband dual-CP antenna characterized by a low profile and structural simplicity. The design features a bilaterally symmetric configuration that integrates a pair of L-shaped microstrip lines and slit-divided rectangular protrusion to achieve wideband dual-CP radiation. A distributed electromagnetic coupling mechanism is employed to effectively enhance the operating bandwidth. Fabricated on a single-layer substrate, the antenna maintains a low profile. The measured results agree well with the simulations, validating the design advantages in terms of structural simplicity, low cost, and wideband performance. These merits demonstrate the antenna's strong potential for use in coal mine communication systems.

2. ANTENNA DESIGN AND ANALYSIS

2.1. Antenna Structure

Figure 1 shows the configuration of the proposed dual-CP antenna. The antenna was printed on a square FR-4 substrate ($\varepsilon_r = 4.4$, $\tan\delta = 0.02$), with overall dimensions of $40\,\text{mm} \times 40\,\text{mm} \times 0.8\,\text{mm}$. It consists of two L-shaped microstrip feed ports (Port 1 and Port 2) printed on one side of the substrate, and a metal ground plane on the other side. A circular slot with a rectangular protrusion at its bottom was etched on the ground. The rectangular protrusion is split by a narrow rectangular slit.

When Port 1 is excited (with Port 2 matched), the y-polarized wave leads its x-polarized counterpart by 90°, producing LHCP radiation. Conversely, exciting Port 2 (with Port 1 matched) reverses the phase lead, yielding the RHCP. Owing to the structural symmetry, the antenna performance was analyzed only for the Port 1 excitation case.

2.2. Evolution of the Antenna

To explain the design process of the proposed antenna, the evolutionary stages are shown in Fig. 2, and the relevant parameters are listed in Table 1. The simulated results, including S-parameters, amplitude ratio, phase difference between the two orthogonal electric fields (E_x, E_y), and AR, are shown in Fig. 3.

To achieve dual-CP operation, Ant. 1 utilizes a feeding structure comprising symmetrical L-shaped microstrip lines. The CP handedness is controlled by selecting the excitation port. To balance resonant frequency control with low-profile requirements, a square radiator with a single-layer substrate is em-

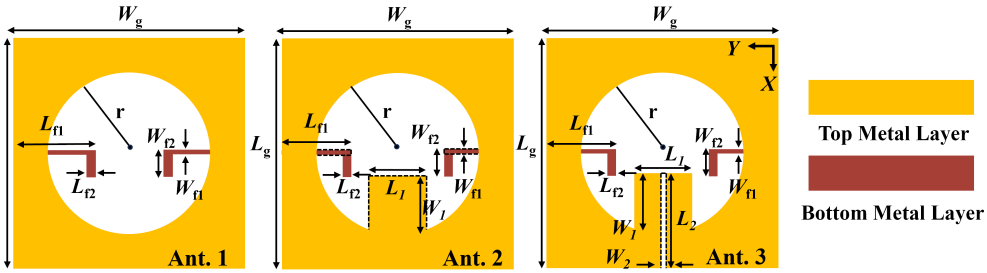

FIGURE 2. Steps to realize the proposed antenna (Ant. 1–3).

TABLE 1. Evolution comparison of geometric parameters of antenna structures.

Parameter	Ant. 1	Ant. 2	Ant. 3	Unit
$L_g = W_g$	40	40	40	mm
r	14	14	14	mm
L_1	\	10	10	mm
W_1	\	12	12	mm
L_2	\	\	18	mm
W_2	\	\	2	mm
L_{f1}	14	13	13	mm
W_{f1}	0.8	0.8	0.8	mm
L_{f2}	2	2	2	mm
W_{f2}	4	4	4	mm
H	0.8	0.8	0.8	mm

ployed. This design incorporates a slot to lengthen the surface current path for bandwidth enhancement. A circular slot is chosen to maintain structural symmetry and simplify the parametric analysis. Thus, Ant. 1 consists solely of two L-shaped microstrip feed lines and a circular slot ground structure. It generates a single resonance at 6.3 GHz. Due to an insufficient electric field component in the x-direction (E_x), the antenna exhibits dual-linear polarization (dual-LP) within the frequency band of 5.63–7.00 GHz, exhibiting poor port isolation around the center frequency. To achieve CP radiation, Ant. 2 incorporates a rectangular metallic protrusion on the x-axis of its circular slot. This element effectively compensates for the E_x, thus creating an AR minimum at 4.4 GHz and enabling a CP band of 3.29–5.31 GHz. Concurrently, this structure excites two resonant frequencies at 4.05 GHz and 6.15 GHz, significantly expanding the IBW to 3.14–7.79 GHz. Furthermore, to enhance port isolation, the lengths of both microstrip lines are reduced to $L_{f1} = 13$ mm. This modification increases the physical separation between the ports, thereby improving the isolation to 10.62 dB. To further improve the isolation performance, Ant. 3 integrates a rectangular narrow slit (18 mm × 2 mm) to separate the metallic protrusion. This slit effectively suppresses the current coupling near the feeding port, thereby improving the port isolation to greater than 12 dB. Additionally, the introduction of the slit excites a new AR minimum at 2.8 GHz, which further optimizes ARBW. Ultimately, the proposed antenna achieves a wide IBW of 2.98–7.68 GHz and a broad ARBW of 2.72–5.47 GHz, maintaining a compact size and excellent radiation performance.

2.3. Theoretical Analysis

(1) Dual-CP

The antenna employs a left-right symmetric geometry, which confers symmetry to its dual-CP properties. This section details the operating principle under the excitation of Port 1, which generates an LHCP wave. By symmetry, exciting Port 2 produces an RHCP wave, thus enabling a dual-CP operation.

A rectangular protrusion was introduced in Ant. 2 to enhance the x-directed electric field component, thereby generating an AR minimum at 4.4 GHz. The surface current on the antenna flows in multiple directions. However, certain current components cancel each other out, as indicated by the dashed black loops. The dominant current directions are indicated by solid black arrows. The surface current distributions across the four phase states after superposition are shown in Fig. 4. The resulting current direction, highlighted by a red arrow in each subfigure, rotates clockwise with increasing phase, confirming LHCP. The CP radiation originates mainly from the ground plane with a rectangular protrusion.

To further broaden ARBW while enhancing port isolation, a narrow rectangular slit was introduced in Ant. 3 to separate the rectangular protrusion completely. This slit forced the current to flow along the segmented sections. The current $\vec{J}_x$ on the left metal protrusion primarily generated the vertical electric field component E_x, whereas the current $\vec{J}_y$ on the horizontal arm of the L-shaped microstrip line was responsible for the horizontal electric field component E_y. The key to achieving CP radiation is that when the current $\vec{J}_y$ couples from the horizontal arm across the gap to the rectangular protrusion, it introduces a phase delay of approximately 90°. This mechanism is strongly confirmed by Fig. 3(d), which shows the phase difference between the orthogonal electric field components E_x and E_y. In Ant. 3 at 2.8 GHz, the phase difference is approximately −90°, which satisfies the necessary condition for circular polarization radiation. Fig. 5(a) shows the current distribution of the antenna at 2.8 GHz. The solid black arrows indicate the current direction. The current rotates clockwise during one oscillation cycle, exhibiting LHCP characteristics. The LHCP radiation was jointly generated by the L-shaped microstrip line and the left segment of the truncated metallic protrusion.

At 4.2 GHz, the enhanced coupling activates a more complex mode, where the other L-shaped microstrip line also acts as a radiator. This generates the horizontal electric field component E_y, while the rectangular protrusion continues to supply E_x. Their interplay results in a new AR minimum, thereby broaden-

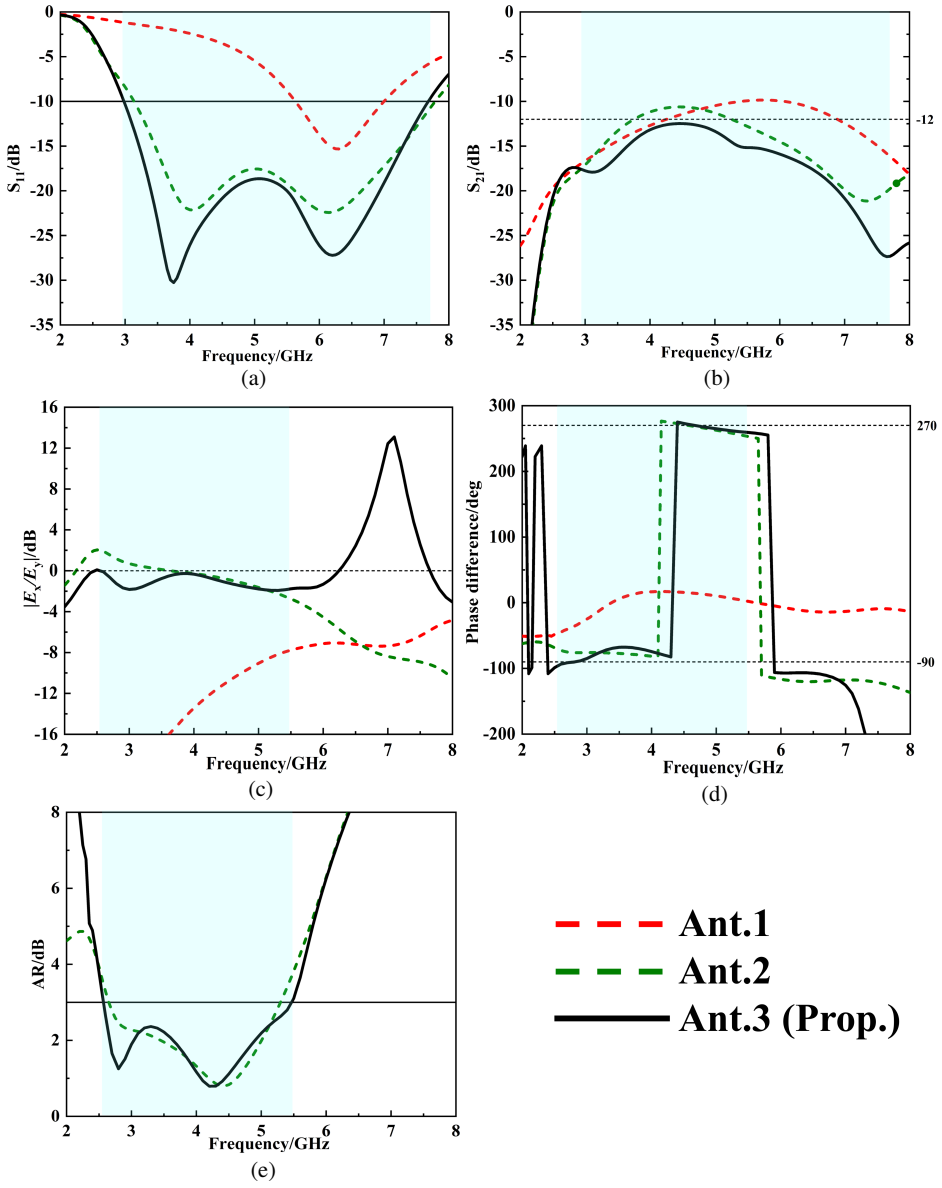

FIGURE 3. Simulated results of Ant. 1–3. (a) S_{11}, (b) S_{21}, (c) amplitude ratio (E_x/E_y), (d) phase difference, and (e) AR.

ing ARBW. As shown in Fig. 5(b), the multi-directional surface currents (black dashed arrows) are superimposed to form dominant paths (red solid arrows) after partial cancellation. These resultant currents rotate clockwise over one full cycle, demonstrating the LHCP characteristics.

The rectangular protrusion acted as a continuous conductor, providing a shared current path for the two symmetric L-shaped microstrip lines. Consequently, this configuration results in strong coupling between ports. The introduced narrow slit physically breaks the current path, as illustrated in Fig. 6. This modification physically eliminates the primary coupling mechanism, thereby achieving port isolation greater than 12 dB. The final design achieved an ARBW of 2.72–5.47 GHz (66.9%).

(2) Wideband

Ant. 1 uses a circular slot fed by an L-shaped microstrip line, generating a resonance near 6.3 GHz. Fig. 7(a) shows the surface current distribution of Ant. 1 at the resonant frequency. The current was primarily concentrated on the dual L-shaped microstrip lines and the left edge of the circular slot. This structural simplicity supports only a single current mode, which leads to a narrow IBW. In Ant. 2, a rectangular protrusion is incorporated at the bottom of the circular slot. This modification created a significant additional current path and successfully excited a second resonant mode at 4.05 GHz. As illustrated in Figs. 7(b) and (c), at 4.05 GHz, the current flows from both sides of the slot toward the corresponding sides of the protrusion. At a higher frequency of 6.15 GHz, the current distribution on the left side of the slot was similar to that of Ant. 1. However, owing to structural modification, the current on the right side was substantially enhanced. The current flowing toward the rectangular protrusion primarily originates from the left L-shaped microstrip line.

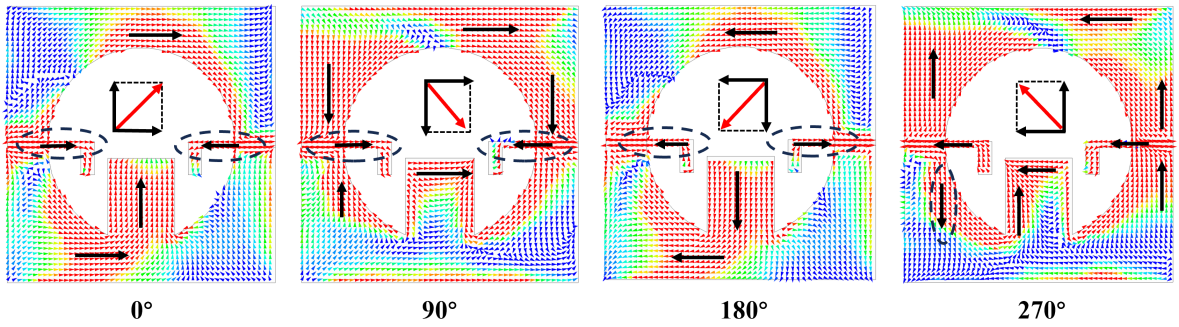

FIGURE 4. Surface current distributions of Ant. 2 at 4.4 GHz.

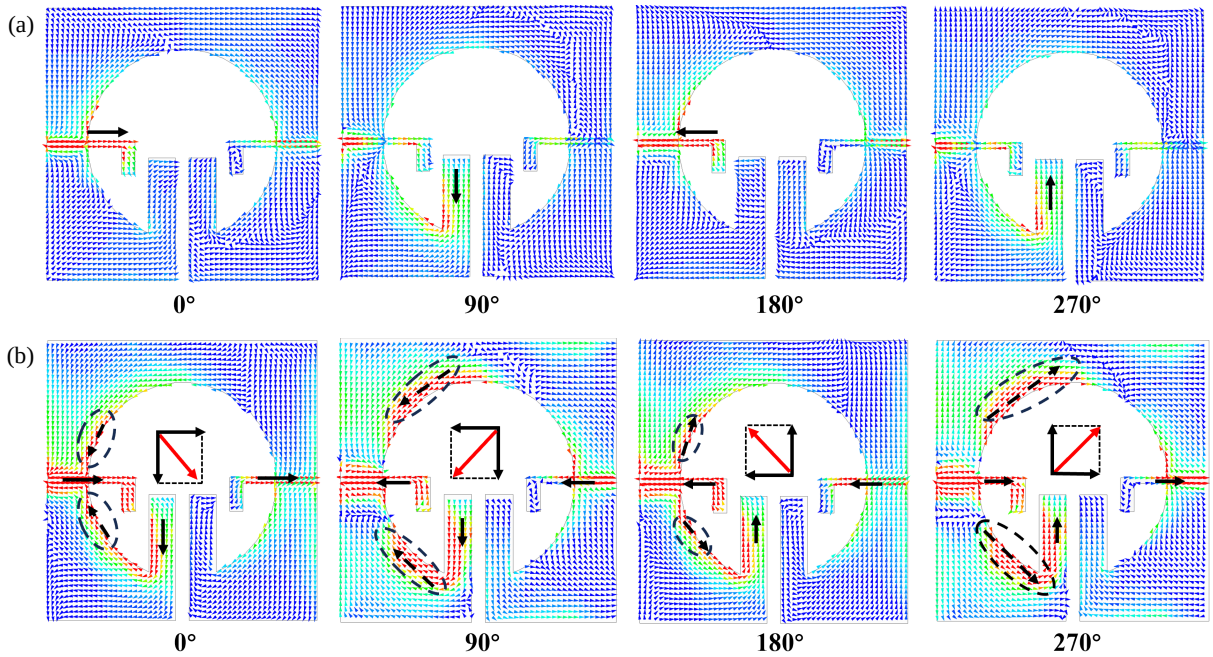

FIGURE 5. Surface current distributions of the proposed antenna. (a) At 2.8 GHz, (b) at 4.2 GHz.

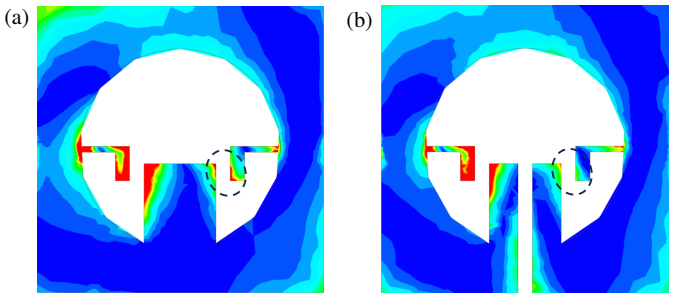

FIGURE 6. Comparative antenna electric field magnitude distributions at resonant frequency: (a) without rectangular slit, (b) with rectangular slit.

In the proposed antenna, the rectangular protrusion is divided into two sections by a narrow slit. This slit not only splits the protrusion, but also contributes to radiation through its own edges. However, the corresponding current distribution was similar to that of Ant. 2, indicating that the radiation mechanism is preserved and that the protrusion still plays a dominant role. Consequently, the primary radiation mechanism was preserved, with only a slight shift in the resonant frequency. This final adjustment tunes the antenna's resonant points to 3.8 GHz and 6.2 GHz. As shown in Figs. 7(d) and (e), at a lower frequency of 3.8 GHz, the current was concentrated mainly along the L-shaped microstrip line and the edge of the circular slot, flowing from both the left and right sides of the slot to the two separated parts of the rectangular protrusion. At a higher frequency of 6.2 GHz, the current couples through the narrow slot between the left and right metallic parts, despite the current distribution along the circular slot edge remaining similar to that shown in Fig. 7(c). This forms multiple parallel radiating paths, each of which operates at a distinct resonant frequency. This distributed coupling mechanism is exploited to extend the bandwidth.

Furthermore, the design of the L-shaped microstrip line provides a smooth impedance transition. The vertical arms of the dual L-shaped microstrip lines achieve tight coupling with the rectangular protrusion, which reduces energy reflection. As a result, excellent impedance matching was maintained across a wide band from 2.98 to 7.68 GHz.

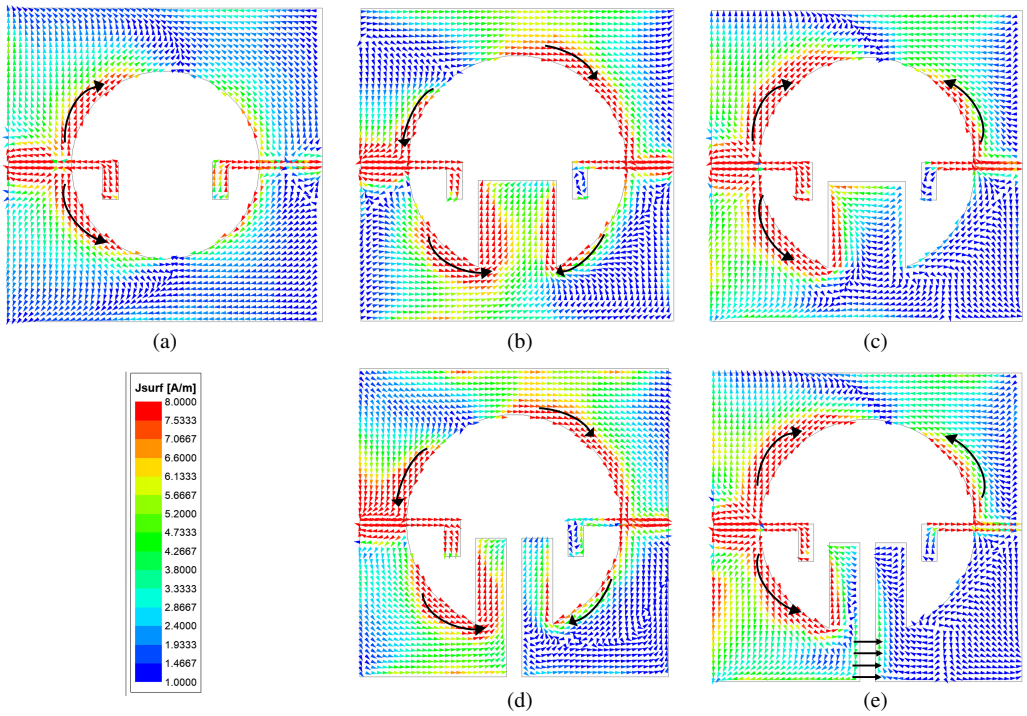

FIGURE 7. Surface current distribution at resonant frequency. (a) Ant. 1 at 6.3 GHz, (b) Ant. 2 at 4.05 GHz, (c) Ant. 2 at 6.15 GHz, (d) Ant. 3 at 3.8 GHz, (e) Ant. 3 at 6.2 GHz.

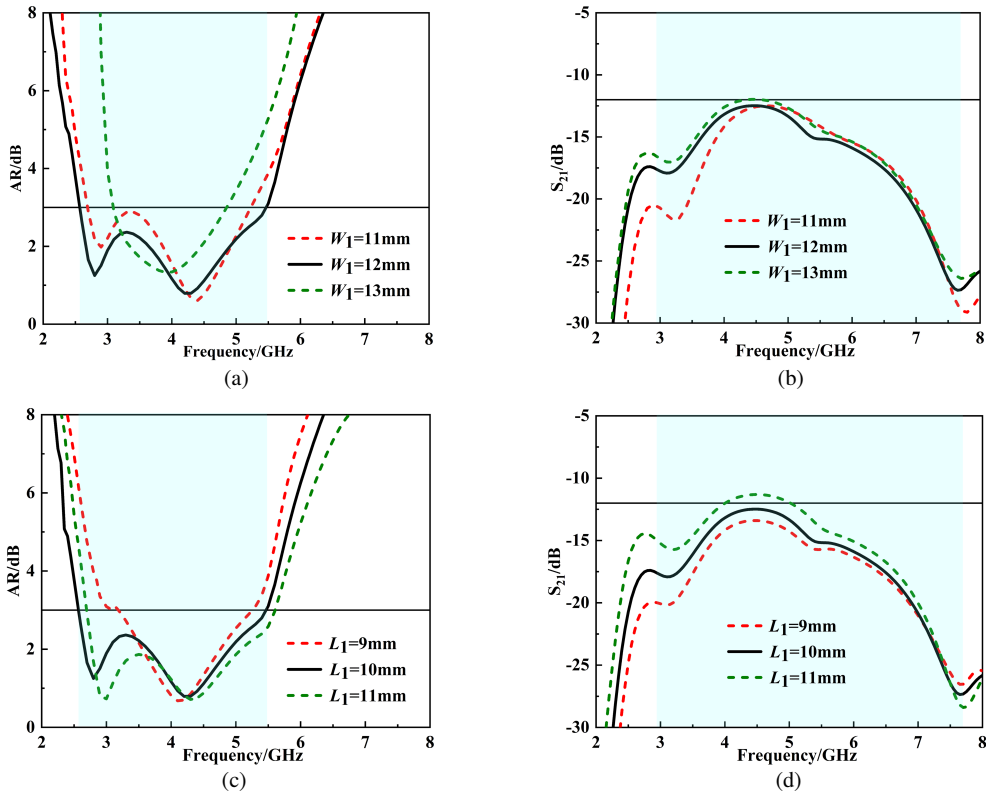

FIGURE 8. The simulated AR and S_{21}. (a), (b) Different values of W_1. (c), (d) Different values of L_1.

2.4. Parametric Study and Discussion

A parametric study was conducted to investigate the influence of the key dimensions on antenna performance. Because the rectangular protrusion ($W_1 \times L_1$) loaded at the bottom of the circular slot is crucial for generating CP radiation, its dimensions were optimized. As shown in Fig. 8(a), increasing W_1

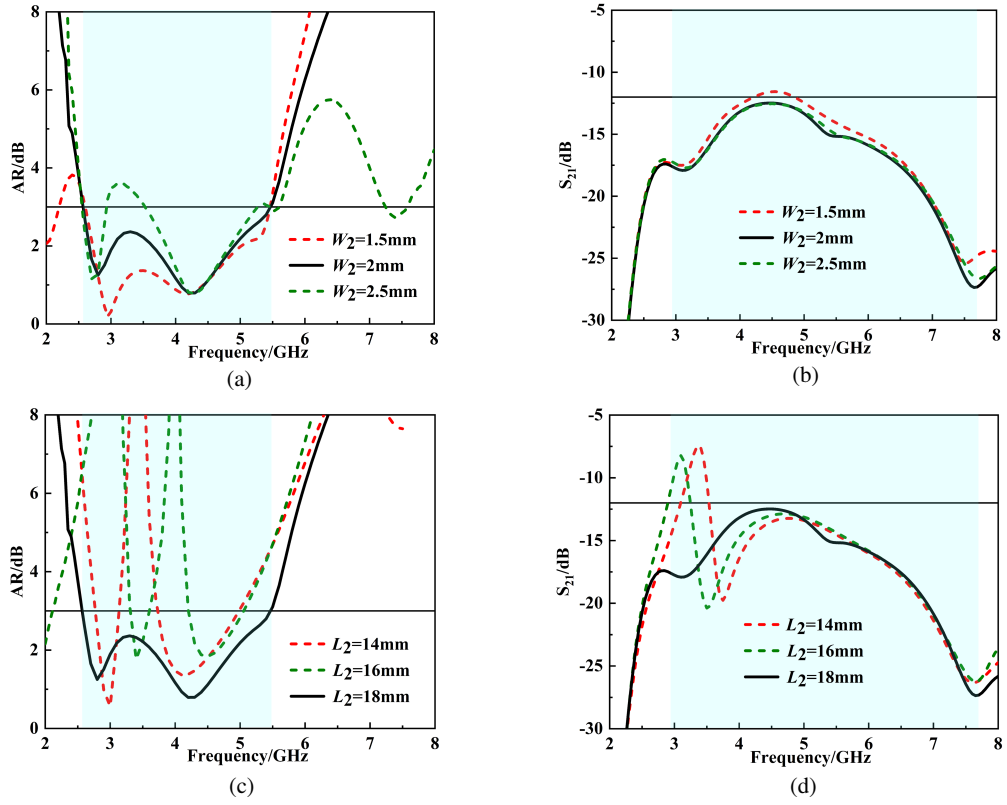

FIGURE 9. The simulated AR and S_{21}. (a), (b) Different values of W_2. (c), (d) Different values of L_2.

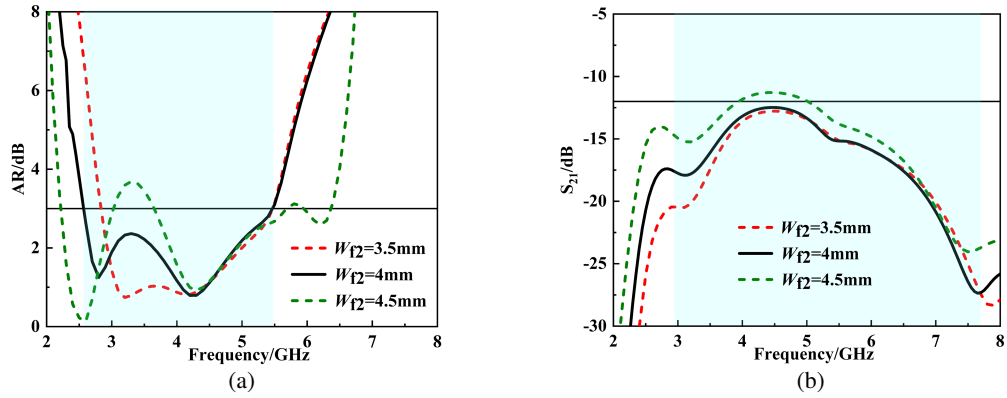

FIGURE 10. Simulation result comparison of AR and S_{21} for the proposed antenna with varying W_{f2} values. (a) AR, (b) S_{21}.

narrows the ARBW, whereas Fig. 8(b) indicates that it also reduces port isolation. A value of $W_1 = 12$ mm was selected for optimal performance. The analysis showed that the length L_1 critically affects both ARBW and isolation. Reducing L_1 improves isolation but narrows ARBW, as shown in Figs. 8(c) and (d), because L_1 controls the coupling intensity. Therefore, $L_1 = 10$ mm was selected as the optimal compromise.

The slit dimensions ($W_2 \times L_2$) are the key parameters. While a smaller W_2 improves CP radiation, it degrades the port isolation owing to excessive energy coupling. As shown in Figs. 9(a) and (b), a comprehensive trade-off identifies $W_2 = 2$ mm as the optimal value. Additionally, Figs. 9(c) and (d) show that an AR passband (2.57–5.47 GHz) with port isolation greater than 12 dB is achieved only when $L_2 = 18$ mm, which is a length that completely truncates the rectangular protrusion.

The width W_{f2} of the L-shaped microstrip line's vertical arms governs their coupling to the protrusion. As shown in Figs. 10(a) and (b), when W_{f2} decreases, the coupling weakens, thereby narrowing the ARBW. When W_{f2} increases, not only is an AR passband no longer formed, but the inter-port coupling is also intensified, thereby degrading isolation. Therefore, $W_{f2} = 4$ mm was chosen to achieve the best balance between ARBW and isolation performance.

In summary, ARBW and port isolation can be tuned by adjusting the rectangular protrusion, narrow slit, and L-shaped microstrip line. This correlation, which is consistent with the

TABLE 2. Comparison of this paper with other research results.

Ref.	IBW (%)	ARBW (%)	Iso (dB)	Size (λ_0)	Polarization
[10]	68.1	57.8	/	$0.85 \times 0.85 \times 0.11$	LHCP
[14]	46	37.7	/	$0.93 \times 0.93 \times 0.06$	RHCP
[17]	113.7	101.3	/	$0.41 \times 0.41 \times 0.17$	LHCP
[23]	29.5	28.6	> 15	$0.41 \times 0.41 \times 0.119$	LHCP&RHCP
[24]	30	29.1	> 10	$0.77 \times 0.56 \times 0.07$	LHCP&RHCP
[25]	23	23	> 27	3.47×3.47	LHCP&RHCP
[26]	104	100	> 30	$0.48 \times 0.48 \times 0.16$	LHCP&RHCP
[27]	39.2	35	> 17	$\pi \times 8.3 \times 0.21$	LHCP&RHCP
[28]	52.5	31.3	> 10	$0.71 \times 0.71 \times 0.04$	LHCP&RHCP
[29]	81.7	59.65	> 15	$0.6 \times 0.6 \times 0.016$	LHCP&RHCP
[30]	108	92.6	> 10	$0.61 \times 0.61 \times 0.006$	LHCP&RHCP
This work	87.8	59.5	> 12	$0.56 \times 0.56 \times 0.011$	LHCP&RHCP

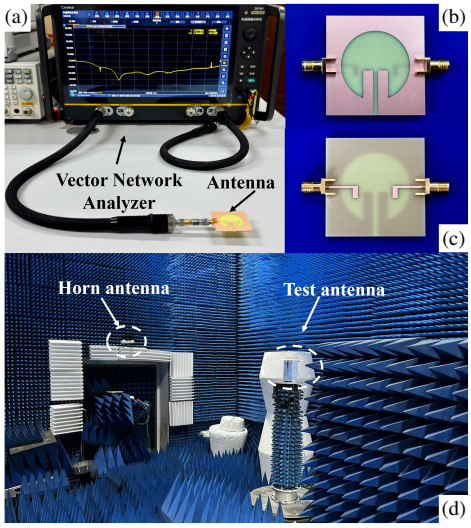

FIGURE 11. The details of the fabricated antenna. (a) Testing scenario, (b) top view, (c) bottom view, (d) radiation pattern testing scenario.

prior analysis, offers a simplified design process and greater optimization flexibility.

3. SIMULATION AND MEASURED RESULTS

The fabricated prototype of the proposed antenna is illustrated in Fig. 11. The simulated and measured S-parameters are presented in Figs. 12(a) and (b), respectively. The measured results demonstrate an IBW of 87.8% (2.98–7.65 GHz), with port isolation greater than 12 dB across this band. The measured and simulated ARs and gains are compared in Fig. 13. The measured 3-dB ARBW was 66.9% (2.72–5.47 GHz), with a peak gain of 5.7 dBic within the overlapping band. The close agreement between simulation and measurement validates the design, whose bandwidth meets the practical requirements for communication systems in the mining industry.

As illustrated in Fig. 11(d), the radiation patterns of the antenna were measured in an anechoic chamber. All collected data underwent system calibration and path loss compensation. The processed normalized radiation patterns in the xoz- and xoy-planes at 2.8 GHz and 4.2 GHz are presented in Fig. 14. The antenna exhibits bidirectional radiation: when Port 1 is excited (Port 2 terminated), it radiates LHCP waves in the $+z$-direction and RHCP waves in the $-z$-direction. Due to structural symmetry, the RHCP patterns under Port 2 excitation are omitted. The polarization isolation exceeded 15 dB, demonstrating excellent bidirectional dual-CP radiation across the operating band.

To better demonstrate the characteristics of this antenna, Table 2 summarizes a comparison between the proposed antenna and other CP antennas. Although Refs. [10, 14, 17] achieved a relatively wide ARBW, they could only realize single CP radiation. Compared to [24, 28], the proposed antenna exhibits superior performance in terms of bandwidth, isolation, and profile. Although the port isolation is lower than that of [23, 25, 27], the proposed antenna offers superior bandwidth and a more compact profile. While Ref. [26] achieved a wide bandwidth along with high port-to-port isolation, and it featured a higher profile, which is detrimental to integration. Furthermore, it employs a quadrature wideband coupler, resulting in a more complex design. The proposed design is a slot antenna, similar to that in [29, 30]. The key innovation of this study lies in achieving an 87.8% IBW, a 59.5% ARBW, and > 12 dB isolation in a compact, low-profile ($0.011\lambda_0$), and easily integrable structure. This design demonstrates an excellent balance among low profile, wide bandwidth, and high isolation. The adoption of a low-cost FR-4 substrate and fabrication process lowers the manufacturing cost while maintaining good performance. Consequently, the antenna is highly suitable for portable coal mine communication devices with strict requirements for cost, size, and bandwidth.

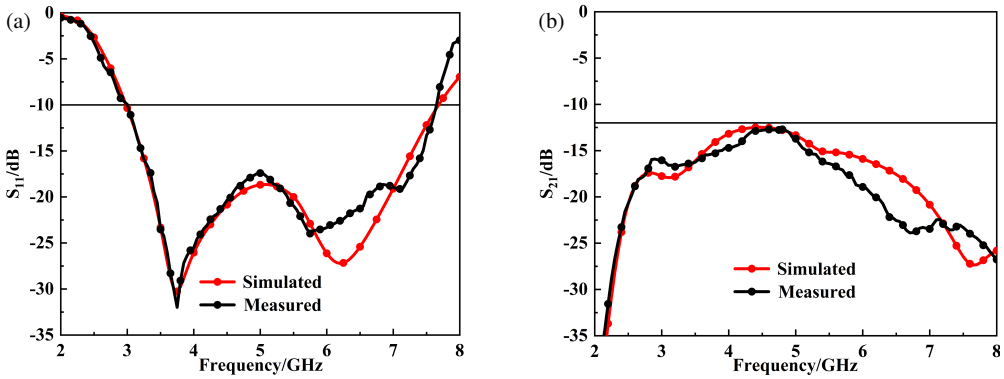

FIGURE 12. Simulated and measured results of the proposed antenna. (a) S_{11}, (b) S_{21}.

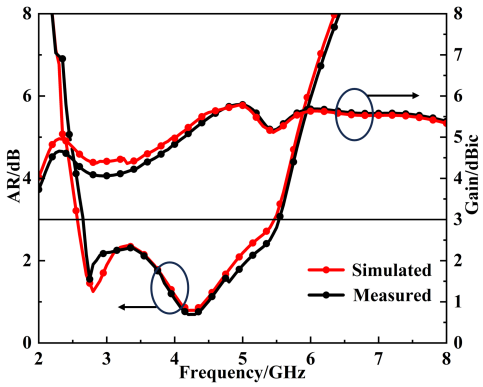

FIGURE 13. Simulated and measured results of the proposed antenna. (a) AR, (b) gain.

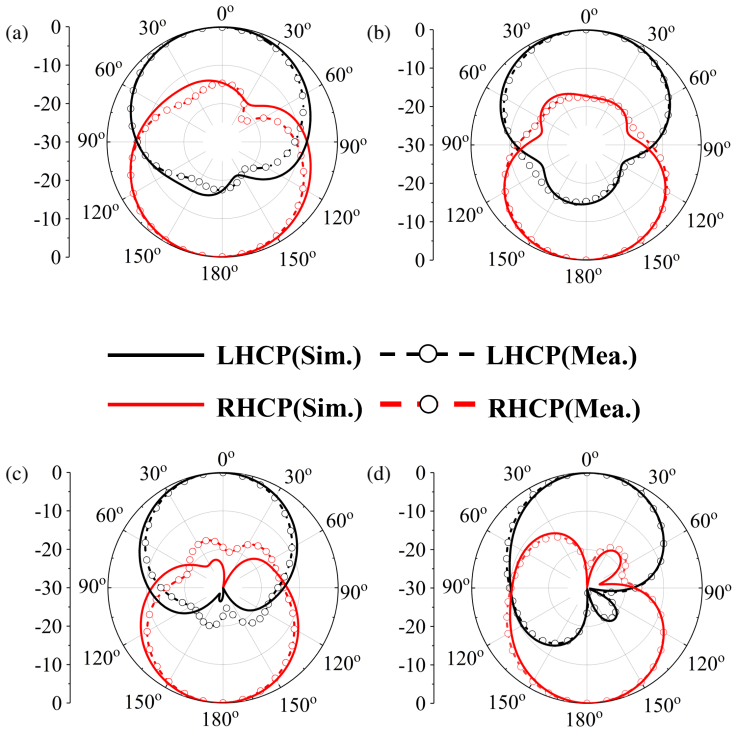

FIGURE 14. Simulated and measured radiation patterns at 2.8 and 4.2 GHz: (a) 2.8 GHz, xoy-plane, (b) 2.8 GHz, xoz-plane, (c) 4.2 GHz, xoy-plane, (d) 4.2 GHz, xoz-plane.

4. CONCLUSION

In this study, a low-profile, wideband dual-CP antenna was designed and implemented. The design employed a symmetrical structure fed by dual L-shaped microstrip lines to generate two orthogonal field components, thus achieving effective dual-CP radiation with a stable 90° phase difference across a wide bandwidth. Furthermore, the introduction of a rectangular protrusion and an isolation slit in the ground plane created multiple resonant paths. This distributed electromagnetic coupling mechanism significantly extends the operating bandwidth while effectively enhancing the port-to-port isolation. The antenna features a compact structure, with overall dimensions of $0.56\lambda_0 \times 0.56\lambda_0 \times 0.01\lambda_0$. A prototype is fabricated and measured to validate the design. The measured results demonstrate an overlapping bandwidth of 59.5% (2.98–5.47 GHz), which effectively covers the civil ultra-wideband (UWB) (3.1–4.8 GHz) for underground coal mines, the 5G NR band (4.8–4.9 GHz), and the WiFi-6 band (5 GHz). The proposed wideband dual-CP antenna offers a simple structure, making it highly suitable for wideband wireless transmission in complex industrial environments, such as coal mines.

ACKNOWLEDGEMENT

This work was supported by the [Liaoning Provincial Department of Education Basic Research Funding Program] under Grant [LJ232410147074].

REFERENCES

[1] Forooshani, A. E., S. Bashir, D. G. Michelson, and S. Noghanian, "A survey of wireless communications and propagation modeling in underground mines," *IEEE Communications Surveys & Tutorials*, Vol. 15, No. 4, 1524–1545, 2013.

[2] Wu, Y., M. Chen, K. Wang, and G. Fu, "A dynamic information platform for underground coal mine safety based on internet of things," *Safety Science*, Vol. 113, 9–18, 2019.

[3] Huo, Y., L. Zhao, Q. Hu, E. Ding, X. Zhao, and Z. Sun, "Optimal deployment of antenna for field coverage in coal mine tunnels," *IEEE Access*, Vol. 8, 51 954–51 963, 2020.

[4] Iwasaki, H. and N. Chiba, "Circularly polarised back-to-back microstrip antenna with an omnidirectional pattern," *IEE Proceedings — Microwaves, Antennas and Propagation*, Vol. 146, No. 4, 277–281, 1999.

[5] Lin, W., H. Wong, and R. W. Ziolkowski, "Circularly polarized antenna with reconfigurable broadside and conical beams facilitated by a mode switchable feed network," *IEEE Transactions on Antennas and Propagation*, Vol. 66, No. 2, 996–1001, 2018.

[6] Liu, S., Z. Wang, and Y. Dong, "A compact filtering patch antenna with high suppression level and its CP application," *IEEE Antennas and Wireless Propagation Letters*, Vol. 22, No. 4, 769–773, 2023.

[7] Li, J., H. Liu, S. Zhang, M. Luo, Y. Zhang, and S. He, "A wideband single-fed, circularly-polarized patch antenna with enhanced axial ratio bandwidth for UHF RFID reader applications," *IEEE Access*, Vol. 6, 55 883–55 892, 2018.

[8] Cheng, Y. and Y. Dong, "Wideband circularly polarized split patch antenna loaded with suspended rods," *IEEE Antennas and Wireless Propagation Letters*, Vol. 20, No. 2, 229–233, 2021.

[9] Ding, K., Y. Li, Y. Li, Y. Wu, and J.-F. Li, "Gain-improved wideband circularly polarized magnetoelectric dipole antenna with parasitic helix," *IEEE Transactions on Antennas and Propagation*, Vol. 71, No. 5, 4516–4521, 2023.

[10] He, W., Y. He, S.-W. Wong, and C.-H. Liao, "A wideband circularly polarized S-shaped slot antenna," *International Journal of RF and Microwave Computer-Aided Engineering*, Vol. 31, No. 5, e22612, 2021.

[11] Ellis, M. S., Z. Zhao, J. Wu, X. Ding, Z. Nie, and Q.-H. Liu, "A novel simple and compact microstrip-fed circularly polarized wide slot antenna with wide axial ratio bandwidth for C-band applications," *IEEE Transactions on Antennas and Propagation*, Vol. 64, No. 4, 1552–1555, 2016.

[12] Ullah, U. and S. Koziel, "A broadband circularly polarized wide-slot antenna with a miniaturized footprint," *IEEE Antennas and Wireless Propagation Letters*, Vol. 17, No. 12, 2454–2458, 2018.

[13] Zeng, Y., X. Qing, and M. Y.-W. Chia, "A wideband circularly polarized antenna with a nonuniform metasurface designed via multiobjective Bayesian optimization," *IEEE Antennas and Wireless Propagation Letters*, Vol. 23, No. 6, 1739–1743, 2024.

[14] Han, L., X. Chen, G. Han, Y. Liu, Y. Zhao, and W. Zhang, "A compact broadband circularly polarized metasurface antenna," *Microwave and Optical Technology Letters*, Vol. 67, No. 8, e70347, 2025.

[15] Liu, H., Y. Zhang, and X. Zhao, "A wideband circularly polarized antenna array loaded with dual-layer metasurface," *IEEE Transactions on Antennas and Propagation*, Vol. 72, No. 8, 6717–6722, 2024.

[16] He, Y., W. He, and H. Wong, "A wideband circularly polarized cross-dipole antenna," *IEEE Antennas and Wireless Propagation Letters*, Vol. 13, 67–70, 2014.

[17] Chen, Z., J. Zeng, S. Xu, and J. Wang, "Compact ultra-wideband circularly polarized crossed-dipole antenna with post fence and parasitic elements," *IEEE Antennas and Wireless Propagation Letters*, Vol. 23, No. 10, 3168–3172, 2024.

[18] Zhang, X., K. Wei, Y. Li, and Z. Zhang, "A circularly polarized antenna based on narrowed crossed dipole for smartphone satellite communication," *IEEE Antennas and Wireless Propagation Letters*, Vol. 23, No. 8, 2511–2515, 2024.

[19] Dai, X. W., Y. H. Zhang, W. Yu, L. Liu, and G. Q. Luo, "Dual-wideband dual-circularly polarized reflectarray based on multiresonant structure for K-band and Ka-band applications," *IEEE Antennas and Wireless Propagation Letters*, Vol. 23, No. 2, 868–872, 2024.

[20] Hu, J. and Z.-C. Hao, "Design of a frequency and polarization reconfigurable patch antenna with a stable gain," *IEEE Access*, Vol. 6, 68 169–68 175, 2018.

[21] Zhou, S., F. Yang, S. Xu, and M. Li, "A dual-circularly polarized reconfigurable reflectarray antenna with independent beam scanning capability," *IEEE Transactions on Antennas and Propagation*, Vol. 72, No. 9, 7100–7109, 2024.

[22] Xu, S., Y. Shen, S. Xue, and S. Hu, "26-/39-GHz low-profile dual-circularly-polarized hybrid antenna with integrated single feed," *IEEE Transactions on Antennas and Propagation*, Vol. 71, No. 11, 8548–8555, 2023.

[23] Hou, Y., J. Ding, Y. Zhang, and J. Mao, "A wideband differential dual circularly polarized laminated resonator antenna," *IEEE Antennas and Wireless Propagation Letters*, Vol. 24, No. 5, 1183–1187, 2025.

[24] Ta, S. X., V. C. Nguyen, B.-T. Nguyen-Thi, T. B. Hoang, A. N. Nguyen, K. K. Nguyen, and C. Dao-Ngoc, "Wideband dual-circularly polarized antennas using aperture-coupled stacked patches and single-section hybrid coupler," *IEEE Ac-*

cess, Vol. 10, 21 883–21 891, 2022.

[25] Zhen, W., T. Qingquan, Y. Dong, F. Kuikui, Y. Weiliang, L. Leilei, and L. G. Qing, "A wideband dual circularly polarized Luneburg lens multi-beam antenna feed by dual linearly polarized ME-dipole antennas," *IEEE Transactions on Antennas and Propagation*, Vol. 73, No. 5, 2804–2813, 2025.

[26] Li, J.-F., T. Xu, D.-L. Wu, Z.-X. Hu, G. Zhang, X.-X. Tian, and L.-H. Ye, "A dual-circularly polarized wideband dipole antenna with stable axial-ratio and half-power beamwidths," *IEEE Antennas and Wireless Propagation Letters*, Vol. 22, No. 7, 1701–1705, 2023.

[27] Gao, S. and H. Wong, "A wideband dual-circularly polarized transmitarray antenna based on magnetoelectric dipole elements and source," *IEEE Transactions on Antennas and Propagation*, Vol. 73, No. 6, 3537–3546, 2025.

[28] Liu, S., D. Yang, and J. Pan, "A low-profile broadband dual-circularly-polarized metasurface antenna," *IEEE Antennas and Wireless Propagation Letters*, Vol. 18, No. 7, 1395–1399, 2019.

[29] Saini, R. K. and S. Dwari, "A broadband dual circularly polarized square slot antenna," *IEEE Transactions on Antennas and Propagation*, Vol. 64, No. 1, 290–294, 2016.

[30] Sun, L., W. Sheng, B. Yan, and J. Cui, "Wideband dual circularly polarized coplanar waveguide-fed slot antenna with an arrow-shaped strip," *International Journal of RF and Microwave Computer-Aided Engineering*, Vol. 32, No. 7, e23194, 2022.